

# Modeling the mixing of heated water discharged from a submerged multiport diffuser

## Modélisation du mélange d'un rejet d'eau chaude émis par un diffuseur multipores immergé

DAE GEUN KIM, *Sectional Chief, Water Resources Team, Kumho Engineering Co., Korea*

IL WON SEO, *Associate Professor, Dept. of Civil Eng., Seoul National Univ., Seoul, Korea*

### ABSTRACT

The mixing of heated water which is discharged from a submerged multiport diffuser was analyzed using the three-dimensional grid-based numerical model. The discharge momentum flux is properly incorporated into the model using the concept of a numerical slot diffuser, along with multi-jet theory. Plane or line patch was introduced to impose discharge momentum flux which plays an important role in mixing of the thermal effluent in the near field. The laboratory experimental work has been conducted to investigate mixing characteristics of the coflowing diffuser. A comparison of model simulations with laboratory experiments show that the proposed model properly simulates the shapes of thermal plumes and the distributions of excess temperature. The proposed model properly simulates velocity induced by a coflowing diffuser in proximity to a shoreline boundary, and this is confirmed by Lee's experiments.

### RÉSUMÉ

Le mélange d'une eau chaude rejetée par un diffuseur multipores immergé a été analysé à l'aide d'un modèle numérique tridimensionnel eulérien. Le flux de quantité de mouvement du rejet est correctement représenté dans le modèle par utilisation du concept de diffuseur fente numérique et de la théorie des jets multiples. Nous avons imposé le flux de quantité de mouvement du rejet sous forme plane ou linéaire, ce qui a un rôle important sur le mélange de l'effluent thermique dans le champ proche. Un travail expérimental a été mené pour étudier les caractéristiques de mélange d'un diffuseur à écoulements parallèles. La comparaison des simulations par modèle avec les expériences de laboratoire montre que le modèle proposé simule bien les formes de panaches thermiques et les distributions d'excès de température. Le modèle proposé simule également correctement la vitesse induite par un diffuseur à écoulements parallèles à proximité de la frontière constituée par un rivage, ce que confirme les expérimentations de Lee.

## 1 Introduction

Submerged multiport diffusers are generally thought to be the most effective means of rapidly diluting thermal discharges. The multiport diffuser is a linear diffusion structure consisting of a manifold which contains numerous closely spaced ports through which heated water is discharged as in the form of a turbulent jet into the receiving water at high velocity. By discharging the heated water through a large number of ports at a high velocity, the total area available for jet entrainment is increased, thus, permitting the rapid dilution of the discharged water. Submerged thermal diffusers are characterized by low buoyancy of the discharge under shallow water conditions, and, as a result, vertically fully mixed conditions usually occurs around the diffuser. The flow dynamics in the near field are governed purely by the momentum source represented by the high velocity injection. In the far field, mixing is governed by ambient currents and stratification. Furthermore, processes at the air-water interface, namely heat exchange to the atmosphere and wind stress can further affect the heat distribution.

Because of the wide range of space and time scales over which the mixing processes occur, it is impossible to develop a comprehensive numerical model to cover both the near and far fields. Most analyses address this scale disparity by simply employing separate models for the near field and far field. Near field models, such as CORMIX2 (Akar and Jirka, 1991), UM (Baumgartner et al., 1993), RSB (Roberts et al., 1989 a, b, c) deal with the initial mixing which takes place in a matter of a few minutes and within a range of tens to hundreds of meters.

For the case of far field model, the mixing processes take place in a matter of days to months and within a range of tens or hundreds of kilometers, and grid size of the model is generally in the order of tens to thousands meters. Various far field models have been developed and these have been summarized and categorized by Cheng and Smith (1989) and Davies et al. (1997 a, b). The problem with employing separate models for near and far fields is that interactions of the two fields are not properly taken into consideration.

The grid-based numerical model has been limited use in the analysis of mixing characteristics of heated water discharged from the multiport diffuser. The reason for this is that, using the grid-based numerical model it is difficult to load the buoyancy and momentum fluxes of the heated water appropriately in the model. Therefore, simulations concerning the dynamic effects of heated water are flawed. The majority of grid-based models for the analysis of mixing characteristics of thermal effluent which is discharged from the multiport diffuser have assumed a passive transport of pollutant. However, this assumption is unrealistic for the analysis of thermal diffuser, which is characterized by great momentum flux with low buoyancy of the discharge under conditions of shallow water. Because the dynamic effects in the near field are important for analysis of the thermal diffuser, the results of grid-based model, using this assumption, may be unreasonable.

This study describes an analysis of mixing of thermal effluent discharged from multiport diffuser using the three-dimensional grid-based numerical model. The discharge momentum flux is

Revision received July, 1999. Open for discussion till February 28, 2001.

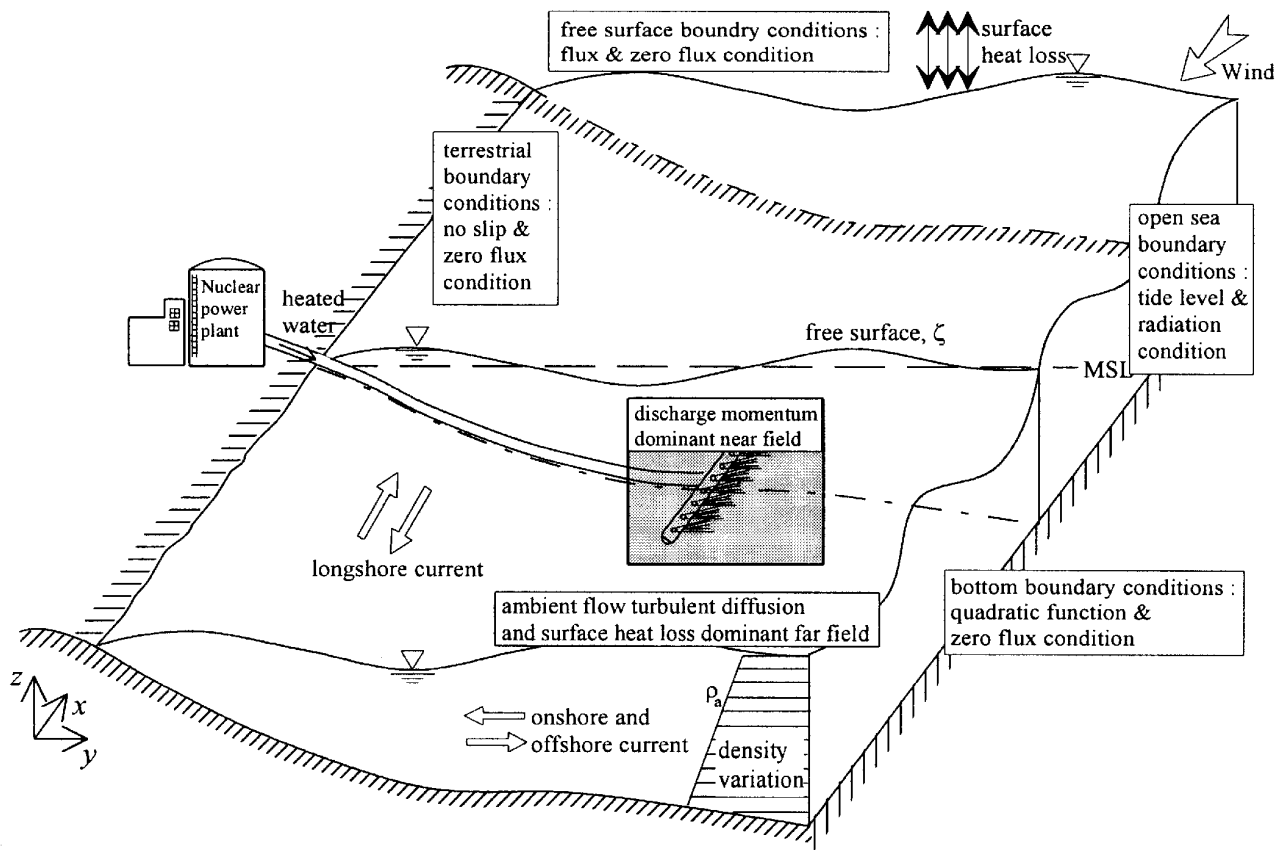


Fig. 1. Schematic depiction of submerged thermal discharge and imposed boundary conditions.

incorporated properly into the model using the concept of numerical slot diffuser. The laboratory experimental work has been conducted to investigate mixing characteristics of the coflowing diffuser. The results of numerical model were compared against experimental data obtained in this study and previous work by Lee (1984).

## 2 Mathematical model

### 2.1 Governing equations

The physical situations considered in this study are described in Fig. 1. The continuity equation, three-dimensional Reynolds equations with Boussinesq's and hydrostatic pressure assumptions, and scalar transport equations can be written as (Blumberg and Mellor, 1987).

$$\frac{\partial U}{\partial x} + \frac{\partial V}{\partial y} + \frac{\partial W}{\partial z} = 0 \quad (1)$$

$$\frac{\partial U}{\partial t} + \frac{\partial(U^2)}{\partial x} + \frac{\partial(UV)}{\partial y} + \frac{\partial(UW)}{\partial z} = fV - \frac{1}{\rho_o} \frac{\partial p}{\partial x} + \frac{\partial}{\partial z} \left( K_v \frac{\partial U}{\partial z} \right) + F_x \quad (2)$$

$$\frac{\partial V}{\partial t} + \frac{\partial(UV)}{\partial x} + \frac{\partial(V^2)}{\partial y} + \frac{\partial(VW)}{\partial z} = -fU - \frac{1}{\rho_o} \frac{\partial p}{\partial y} + \frac{\partial}{\partial z} \left( K_v \frac{\partial V}{\partial z} \right) + F_y \quad (3)$$

$$\frac{\partial p}{\partial z} = -\rho g \quad (4)$$

$$\frac{\partial T}{\partial t} + \frac{\partial(UT)}{\partial x} + \frac{\partial(VT)}{\partial y} + \frac{\partial(WT)}{\partial z} = \frac{\partial}{\partial z} \left( E_v \frac{\partial T}{\partial z} \right) + F_T \quad (5)$$

$$\frac{\partial S}{\partial t} + \frac{\partial(US)}{\partial x} + \frac{\partial(VS)}{\partial y} + \frac{\partial(WS)}{\partial z} = \frac{\partial}{\partial z} \left( E_v \frac{\partial S}{\partial z} \right) + F_S \quad (6)$$

in which  $U$ ,  $V$ , and  $W$  = velocities in the  $x$ ,  $y$ , and  $z$  directions;  
 $f$  = Coriolis' constant;  
 $g$  = gravitational acceleration;  
 $\rho$  = density;  
 $\rho_o$  = reference density;  
 $K_v$  = vertical eddy viscosity;  
 $F_x$ ,  $F_y$  = horizontal viscosity terms;  
 $E_v$  = vertical eddy diffusivity;  
 $T$  = temperature;  
 $S$  = salinity;  
 $F_T$ ,  $F_S$  = horizontal diffusivity terms.

As shown in Fig. 2, converting the conventional Cartesian coordinates to sigma coordinates using relation defined by Eq. (7), the governing equations (Eqs. 1-6) are converted as

$$\sigma = \frac{z - \zeta}{H} \quad (7)$$

$$\frac{\partial \zeta}{\partial t} + \frac{\partial(HU)}{\partial x} + \frac{\partial(HV)}{\partial y} + \frac{\partial \Omega}{\partial \sigma} = 0 \quad (8)$$

$$\frac{\partial(HU)}{\partial t} - \frac{\partial}{\partial \sigma} \left( \frac{K_v}{H} \frac{\partial U}{\partial \sigma} \right) = - \left\{ \frac{\partial(HU^2)}{\partial x} + \frac{\partial(HUV)}{\partial y} + \frac{\partial(U\Omega)}{\partial \sigma} \right\} + fVH - gH \frac{\partial \zeta}{\partial x} \quad (9)$$

$$- \frac{gH^2}{\rho_o} \int_{\sigma}^0 \left( \frac{\partial \rho}{\partial x} - \frac{\sigma}{H} \frac{\partial H}{\partial x} \frac{\partial \rho}{\partial \sigma} \right) d\sigma + F_x$$

$$\frac{\partial(HV)}{\partial t} - \frac{\partial}{\partial \sigma} \left( \frac{K_v}{H} \frac{\partial V}{\partial \sigma} \right) = - \left\{ \frac{\partial(HUV)}{\partial x} + \frac{\partial(HV^2)}{\partial y} + \frac{\partial(V\Omega)}{\partial \sigma} \right\} - fUH - gH \frac{\partial \zeta}{\partial y} \quad (10)$$

$$- \frac{gH^2}{\rho_o} \int_{\sigma}^0 \left( \frac{\partial \rho}{\partial y} - \frac{\sigma}{H} \frac{\partial H}{\partial y} \frac{\partial \rho}{\partial \sigma} \right) d\sigma + F_y$$

$$\frac{\partial(HT)}{\partial t} - \frac{\partial}{\partial \sigma} \left( \frac{E_v}{H} \frac{\partial T}{\partial \sigma} \right) = - \left\{ \frac{\partial(HUT)}{\partial x} + \frac{\partial(HVT)}{\partial y} + \frac{\partial(\Omega T)}{\partial \sigma} \right\} + F_T \quad (11)$$

$$\frac{\partial(HS)}{\partial t} - \frac{\partial}{\partial \sigma} \left( \frac{E_v}{H} \frac{\partial S}{\partial \sigma} \right) = - \left\{ \frac{\partial(HUS)}{\partial x} + \frac{\partial(HVS)}{\partial y} + \frac{\partial(\Omega S)}{\partial \sigma} \right\} + F_S \quad (12)$$

in which  $\zeta$  = water surface elevation;  $H = h + \zeta$ ;  $h$  = bottom topography;  $\Omega$  = velocity in the  $\sigma$  direction. In sigma coordinates system, the number of grid points in the vertical is independent of depth. The horizontal eddy viscosity and diffusivity can be obtained by the Smagorinsky formula which is given by the equation below (Davies et al., 1997 a).

$$K_H = C_s \Delta x \Delta y \left\{ \left( \frac{\partial U}{\partial x} \right)^2 + \left( \frac{\partial V}{\partial x} + \frac{\partial U}{\partial y} \right)^2 + \left( \frac{\partial V}{\partial y} \right)^2 \right\}^{1/2} \quad (13)$$

in which  $K_H$  = horizontal eddy viscosity of horizontal viscosity terms;  $C_s$  = non-dimensional Smagorinsky's constant. In this

study, the same values are used both for horizontal eddy viscosity and diffusivity. Density is related to salinity and temperature by an equation of state (Eckart, 1958). And, then velocity fields are computed using changed density, so dynamically active condition is accounted for in this model.

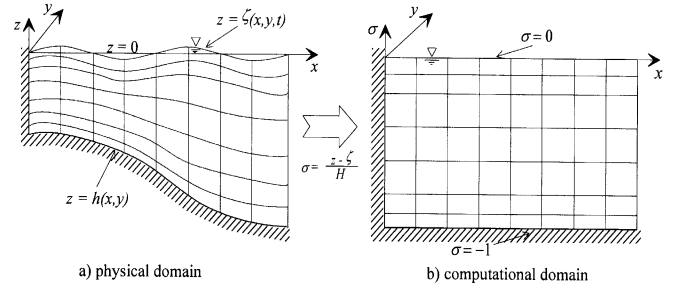


Fig. 2. Transformation of coordinate systems.

The actual  $z$  direction velocity,  $W$ , can be written,

$$W = \Omega + U \left( \sigma \frac{\partial H}{\partial x} + \frac{\partial \zeta}{\partial x} \right) + V \left( \sigma \frac{\partial H}{\partial y} + \frac{\partial \zeta}{\partial y} \right) + \sigma \frac{\partial H}{\partial t} + \frac{\partial \zeta}{\partial t} \quad (14)$$

At the bottom, the stress is specified using the quadratic law with a bottom friction coefficient and zero flux condition is specified for temperature and salinity. At the free surface, a quadratic law is also used to specify the wind stresses, flux condition is specified using heat transfer coefficient for temperature and zero flux condition is specified for salinity.

In general, the equations which govern the dynamics of coastal circulation contain both fast-moving external gravity waves and slow-moving internal gravity waves. Thus, it would be desirable to separate the depth averaged equations (external mode) from the vertical structure equations (internal mode). This technique, known as the mode-splitting method, permits the calculation of the free surface elevation with little sacrifice in computational time. External-mode equations are obtained by integrating the internal-mode equations over the depth. Thus, the integration of Eqs. (8) to (10) from  $\sigma = -1$  to  $\sigma = 0$  and using vertical boundary conditions, equations for continuity and momentum gives;

$$\frac{\partial \zeta}{\partial t} + \frac{\partial(H\bar{U})}{\partial x} + \frac{\partial(H\bar{V})}{\partial y} - \Omega_b = 0 \quad (15)$$

$$\frac{\partial(H\bar{U})}{\partial t} + \frac{\partial(H\bar{U}^2)}{\partial x} + \frac{\partial(H\bar{U}\bar{V})}{\partial y} - f\bar{V}H + gH \frac{\partial \zeta}{\partial x} = \quad (16)$$

$$\frac{\tau_{wx}}{\rho_o} + \frac{\tau_{bx}}{\rho_o} - \frac{gH}{\rho_o} \int_{-1}^0 \left( \frac{\partial \rho}{\partial x} - \sigma \frac{\partial H}{\partial x} \frac{\partial \rho}{\partial \sigma} \right) d\sigma d\sigma + \bar{F}$$

$$\frac{\partial(H\bar{V})}{\partial t} + \frac{\partial(H\bar{U}\bar{V})}{\partial x} + \frac{\partial(H\bar{V}^2)}{\partial y} + f\bar{U}H + gH \frac{\partial \zeta}{\partial y} = \quad (17)$$

$$\frac{\tau_{wy}}{\rho_o} + \frac{\tau_{by}}{\rho_o} - \frac{gH}{\rho_o} \int_{-1}^0 \left( \frac{\partial \rho}{\partial y} - \sigma \frac{\partial H}{\partial y} \frac{\partial \rho}{\partial \sigma} \right) d\sigma d\sigma + \bar{F}_y$$

in which  $\Omega_b$  represents the vertical velocity normal to bottom boundary and overbars denote depth averaging. All of terms on the right-hand side of (16) and (17) are evaluated at each internal time step and then held constant throughout the numerous external time steps.

## 2.2 Turbulence modeling

The  $k$ - $l$  turbulence closure scheme as described by Galperin et al. (1988) and Blumberg et al. (1992) is used to calculate vertical eddy viscosity and diffusivity.

$$\begin{aligned} \frac{\partial(Hq^2)}{\partial t} + \frac{\partial(HUq^2)}{\partial x} + \frac{\partial(HVq^2)}{\partial y} + \frac{\partial(\Omega q^2)}{\partial \sigma} = \\ \frac{\partial}{\partial \sigma} \left( \frac{K_q \partial q^2}{H \partial \sigma} \right) + \frac{2K_v}{H} \left\{ \left( \frac{\partial U}{\partial \sigma} \right)^2 + \left( \frac{\partial V}{\partial \sigma} \right)^2 \right\} \\ + \frac{2gE_v \partial \rho}{\rho_o \partial \sigma} - \frac{2Hq^2}{B_1 l} + F_q \end{aligned} \quad (18)$$

$$\begin{aligned} \frac{\partial(Hq^2 l)}{\partial t} + \frac{\partial(HUq^2 l)}{\partial x} + \frac{\partial(HVq^2 l)}{\partial y} + \frac{\partial(\Omega q^2 l)}{\partial \sigma} = \\ \frac{\partial}{\partial \sigma} \left( \frac{K_q \partial q^2 l}{H \partial \sigma} \right) \\ + E_1 l \left[ \frac{K_v}{H} \left\{ \left( \frac{\partial U}{\partial \sigma} \right)^2 + \left( \frac{\partial V}{\partial \sigma} \right)^2 \right\} + \frac{gE_v \partial \rho}{\rho_o \partial \sigma} \right] - \frac{q^3 \tilde{W}}{B_1} + F_l \end{aligned} \quad (19)$$

in which  $q^2$  = two times the turbulent kinetic energy;  $l$  = turbulence length scale,  $K_q$  = vertical eddy diffusivity;  $F_q$ ,  $F_l$  = horizontal diffusivity term.  $\tilde{W}$  represents the wall proximity function which is defined as

$$\tilde{W} = 1 + E_2 \left( \frac{l}{\kappa z} \right)^2 + E_3 \left( \frac{l}{\kappa(H-z)} \right)^2 \quad (20)$$

in which  $\kappa$  = von Karman constant.

Boundary conditions at the free surface and bottom are given as

$$(q^2(0), q^2 l(0)) = \left( B_1^{2/3} \frac{\tau_w}{\rho_o}, 0 \right) \quad (21)$$

$$(q^2(-1), q^2 l(-1)) = \left( B_1^{2/3} \frac{\tau_b}{\rho_o}, 0 \right) \quad (22)$$

in which  $\tau_b$  = bed shear stress;  $\tau_w$  = wind shear stress

The vertical eddy viscosity coefficients and diffusivities are defined as,

$$(K_v, E_v, K_q) = (qlS_k, qlS_e, qlS_q) + DV_{ref} \quad (23)$$

in which  $DV_{ref}$  = base vertical eddy viscosity and diffusivity. The coefficients are given by,

$$S_k = - \frac{B_1^{-1/3} - A_1 A_2 G_H \left\{ (B_2 - 3A_2) \left( 1 - \frac{6A_1}{B_1} \right) - 3C_1 (B_2 + 6A_1) \right\}}{\{ 1 - 3A_2 G_H (6A_1 + B_2) \} (1 - 9A_1 A_2 G_H)} \quad (24)$$

$$S_e = \frac{A_2 \left( 1 - \frac{6A_1}{B_1} \right)}{1 - 3A_2 G_H (6A_1 + B_2)} \quad (25)$$

$$S_q = 0.2 \quad (26)$$

in which  $G_H$  = Richardson number, which is valid over the region -0.28 to 0.0233. The constants in Eqs. (18) - (25) are listed in Table 1.

Table 1. Constants used in  $k$ - $l$  turbulence model.

$A_1$	$A_2$	$B_1$	$B_2$	$C_1$	$E_1$	$E_2$	$E_3$
0.92	0.74	16.6	10.1	0.08	1.8	1.33	0.25

## 2.3 Heated water loading

In this study, the internal boundary at the diffuser is treated as a line patch (see Fig. 3). The discharge flowrate,  $Q_N$  from a cell of the numerical slot diffuser is determined using the following equation in which the merging of adjacent jets is incorporated (Wood et al., 1993).

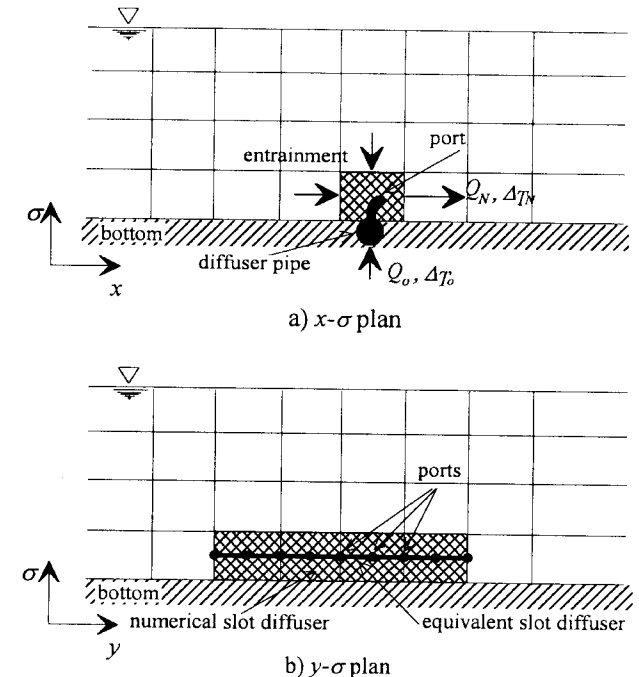


Fig. 3. Internal boundary condition for submerged multiport diffuser.

$$Q_N = nI_q b l U_c \quad (27)$$

in which  $n$  = number of ports included in a cell of the numerical slot diffuser;  $I_q$  = shape constants;  $b$  = effective width of single jet;  $l$  = port spacing;  $U_c$  = jet centerline velocity. In this study, for the shape constants,  $I_q$ , which represent the merging processes of the adjacent jets discharged from the array of linear multiports, the values suggested by Wood et al. (1993) are used. The width of the jet and centerline velocity of each jet can be calculated by following equations, which are based on simple jet theory (Fischer et al., 1979).

$$b = \alpha_1 x \quad (28)$$

$$\frac{U_c}{U_o} = \alpha_2 \frac{l_q}{x} \quad \text{for} \quad \frac{x}{l_q} \geq 7 \quad (29)$$

in which  $U_o$  = outlet velocity;  $l_q$  = characteristic length scale defined as the square root of initial cross sectional area of the jet. The constants,  $\alpha_1$  and  $\alpha_2$  represent coefficients of proportionality of which average values for an ideal single jet are 0.107 and 7.0 respectively. However, adjusted values are used to consider the complex mixing mechanics of a multi-jet. Combining Eq. (27) with Eqs. (28) and (29) results in

$$Q_N = \alpha n I_q l l_q U_o \quad (30)$$

in which  $\alpha = \alpha_1 \alpha_2$ .

The excess temperature,  $\Delta T_N$  from a cell of a numerical slot diffuser can be determined by following equation.

$$\Delta T_N = \frac{Q_o}{Q_N} \Delta T_o \quad (31)$$

in which  $Q_o$  = the discharge flowrate from ports in a cell of the numerical slot diffuser;  $\Delta T_o$  = discharge excess temperature from the multiport diffuser.

#### 2.4 Numerical scheme

The governing equations are solved numerically using the finite difference method. The equations are discretized on so called "Arakawa C" type staggered grid (Blumberg and Mellor, 1987). In this scheme, the horizontal time differencing is explicit whereas the vertical differencing is implicit. The latter eliminates time constraints for the vertical coordinate, thus permitting the use of finer vertical resolution. The external mode portion of the model is two-dimensional and a short time step is used. The internal mode is three-dimensional and a long time step is used. The external-mode calculation results in updates for surface elevation and the depth averaged velocities. The internal-mode calculation results in updates for velocities, scalar and turbulence quantities. In the external mode, Eq. (15) for calculating the free surface is discretized by midpoint leap-frog approximation. The calculation of the internal variables is sepa-

rated into a vertical diffusion time step and an advection plus a horizontal diffusion time step (right-hand side of Eqs. (9), (10), (11), (12)). The former is implicit whereas the latter is explicit. The unsteady term is approximated by the leap-frog method. Flowchart of the computational procedure is depicted in Fig. 4.

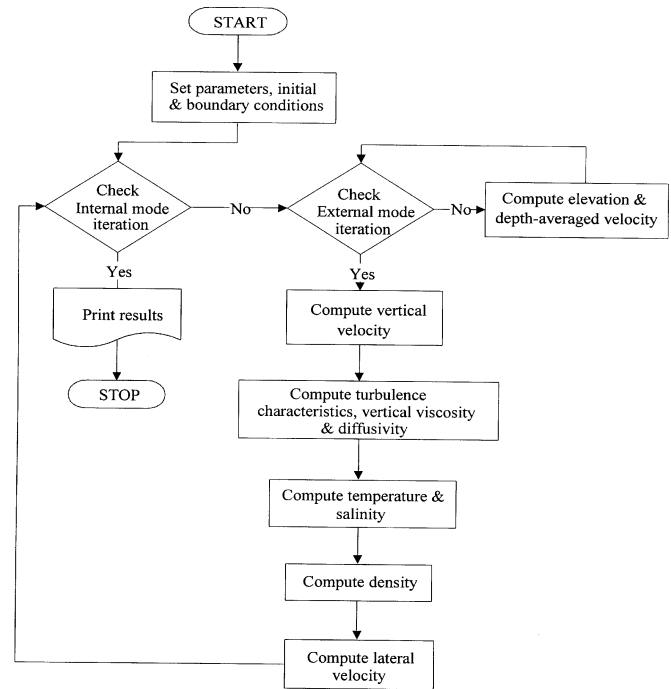


Fig. 4. Flow chart of the computational procedure.

### 3 Laboratory experiments

To investigate mixing characteristics of the coflowing diffuser, the laboratory experiments has been conducted. The coflowing diffuser consists of ports all of which are pointing in one direction and discharging parallel to the ambient crossflow. The geometric configuration of the laboratory model for diffusers was based primarily on diffuser characteristics that have been identified in existing thermal diffuser systems which are currently in operation. Many of these characteristics, such as diffuser length, port diameter and spacing and the ratio of water depth to equivalent slot width, have been summarized by Jirka and Harleman (1973) and Jirka (1982). Even though the characteristics identified in existing thermal diffuser systems were used as the primary criteria in the design of the model diffuser system, the principles of hydraulic similitude were also used as guidelines in determining the appropriate scale of the model. The total length of the model diffuser,  $L_D$ , is 95 cm. The inner diameter of the port is 0.43 cm with a spacing of 5.0 cm. The angle between the port and the channel bottom is, considering the effect of scour, selected as  $22.5^\circ$ .

The physical model of the diffuser system was installed in a 15 m long, 3.5 m wide and 0.35 m deep flume. A schematic diagram of the laboratory flume and the experimental setup is shown in Fig. 5. Flowrate was measured using an electro-magnetic flow meter. Water temperature was measured using CC-Type thermocouple sensors, installed on the instrument carriage. Thermocouple sensors are connected to a 40-channel data

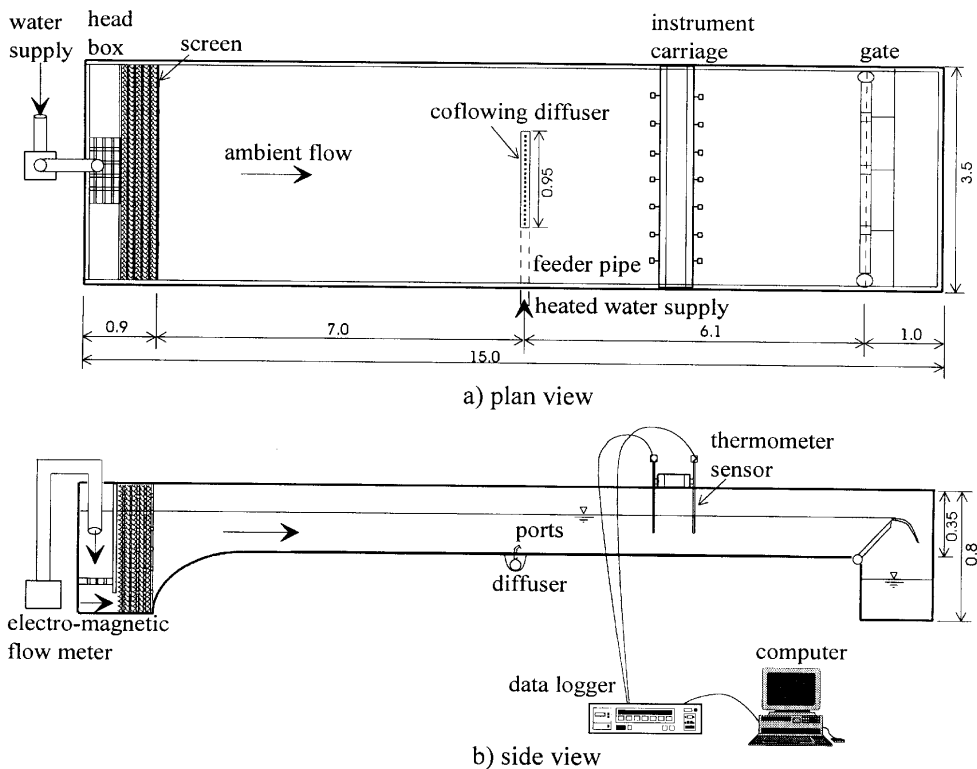


Fig. 5. Schematic diagram of laboratory flume and experimental setup (unit: m).

logger in which measured temperatures are stored in digital form. Thermal effluent was supplied from a specially manufactured hot water bath which consisted of a preheating bath and constant head tank which provided hot water to the diffuser pipe at a constant flowrate.

Experimental cases and conditions for coflowing diffuser are listed in Table 2. In this table,  $u_a$  = ambient current velocity;  $M_r$  = momentum ratio of the ambient current to the effluent discharge;  $B$  = width of equivalent slot diffuser;  $F_s$  = discharge densimetric Froude number of equivalent slot diffuser;  $g'_o$  = effective gravitational acceleration;  $m_o$  = discharge momentum flux per unit length;  $j_o$  = discharge buoyancy flux per unit length, and  $S_m$  = minimum surface dilution observed.

Hydraulic conditions of ambient water, including ambient water depths and ambient velocity, were primarily based on oceanographic conditions of the Korean shore where existing nuclear power plants are sited, in which momentum ratio of the ambient current to the effluent discharge are quite high. Thus, in this experiment the emphasis is focused on the condition of strong ambient current. In this experiment, the ratio of ambient momentum to discharge momentum,  $M_r$ , ranges from 0.28 to 38.3.

As shown in this table, buoyancy flux of the heated water discharge ( $j_o$ ) is relatively small compared to discharge momentum flux ( $m_o$ ). Thus buoyancy effect of the heated water discharge is small in the near field, and vertically well-mixed condition might be assumed in the near field (Jirka, 1982). In the far field, once the discharge momentum is diminished, buoyancy starts to affect the flow field, then density re-stratification usually occurs.

Table 2. Summary of experiential conditions for coflowing diffuser.

Case	$H$ (cm)	$u_a$ (cm/s)	$U_o$ (cm/s)	$M_r$ ( $=u_a^2 u / u_o^2 B$ )	$F_s$ ( $=U_o / \sqrt{g'_o B}$ )	$m_o$ ( $=u_o j_o B$ )	$j_o$ ( $=U_o g'_o B$ )	$S_m$
CO-01	10	2	30	1.53	112.30	26.14	2.14	16.6
CO-02	10	2	50	0.55	187.17	72.61	3.57	19.3
CO-03	10	2	70	0.28	262.04	142.32	5.00	14.5
CO-04	10	6	30	13.77	112.30	26.14	2.14	74.6
CO-05	10	6	50	4.96	187.17	72.61	3.57	32.7
CO-06	10	6	70	2.53	262.04	142.32	5.00	38.5
CO-07	10	10	30	38.26	112.30	26.14	2.14	77.5
CO-08	10	10	50	13.77	187.17	72.61	3.57	38.5
CO-09	10	10	70	7.03	262.04	142.32	5.00	33.8
CO-10	15	2	30	2.30	112.30	26.14	2.14	40.0
CO-11	15	2	50	0.83	187.17	72.61	3.57	25.6
CO-12	15	2	70	0.42	262.04	142.32	5.00	27.8
CO-13	15	6	50	7.44	187.17	72.61	3.57	62.5
CO-14	15	6	70	3.79	262.04	142.32	5.00	63.3
CO-15	20	2	30	3.06	112.30	26.14	2.14	41.7
CO-16	20	2	50	1.10	187.17	72.61	3.57	37.0
CO-17	20	2	70	0.56	262.04	142.32	5.00	45.9
CO-18	20	6	30	27.54	112.30	26.14	2.14	57.1
CO-19	20	6	50	9.92	187.17	72.61	3.57	69.4
CO-20	20	6	70	5.06	262.04	142.32	5.00	51.3

In this experiments, main focus was on the measurements of the temperature field on the water surface near the diffuser. Among the twenty experimental cases, six typical data of observed temperature distributions at the water surface along with simulated results are shown in Fig. 6. In this figure,  $\Delta T$  = excess temperature which is difference between the point temperature meas-

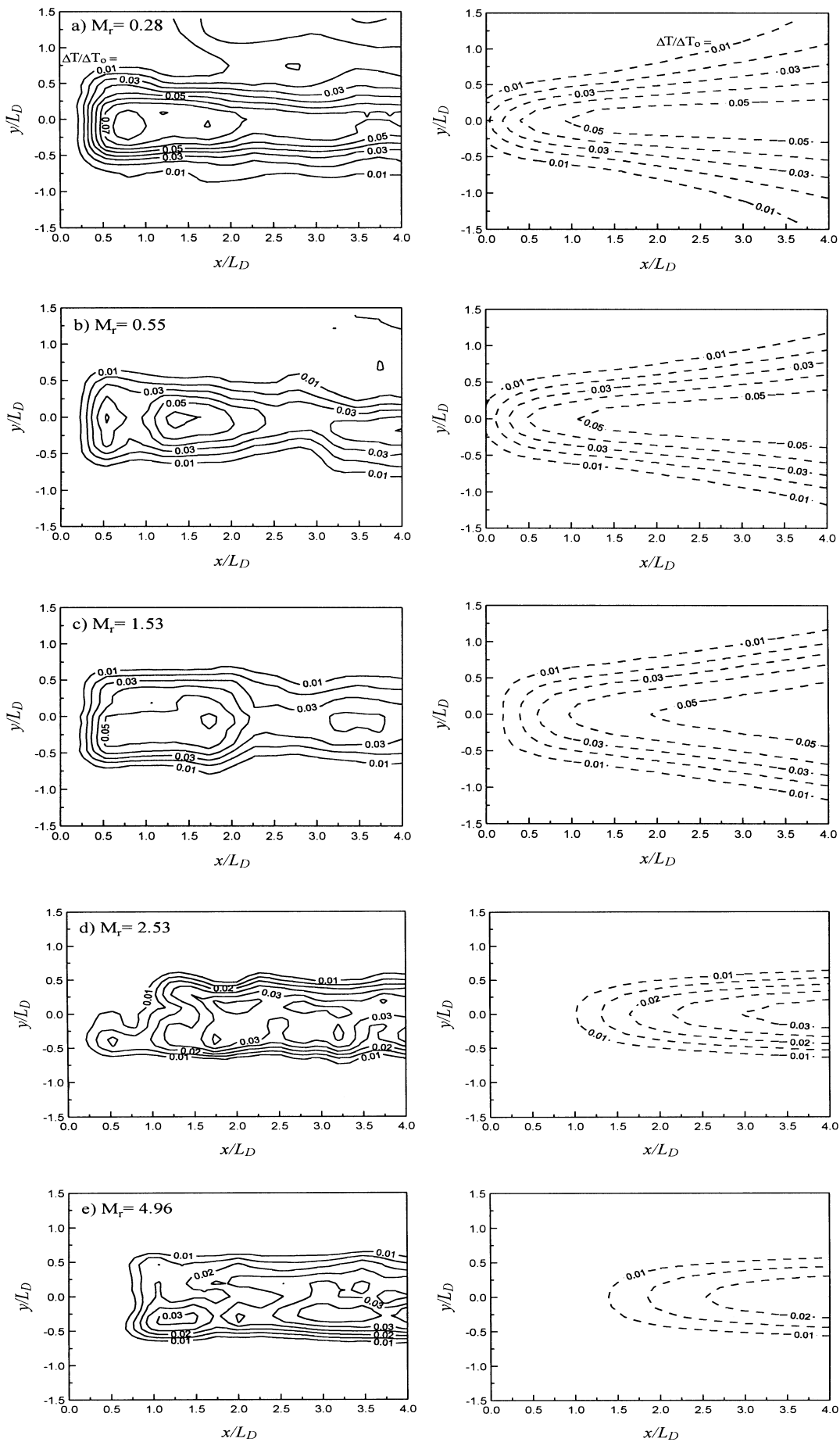


Fig. 6. Comparison of dimensionless excess temperature distribution at water surface: \_\_\_ measurements; - - - simulations.

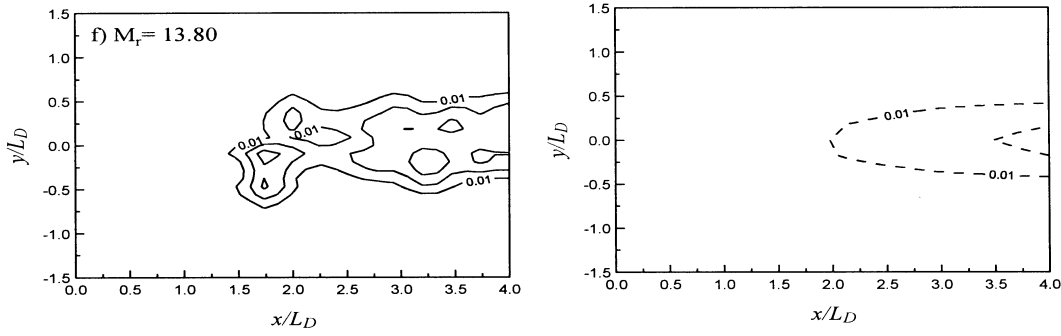


Fig. 6. (continue).

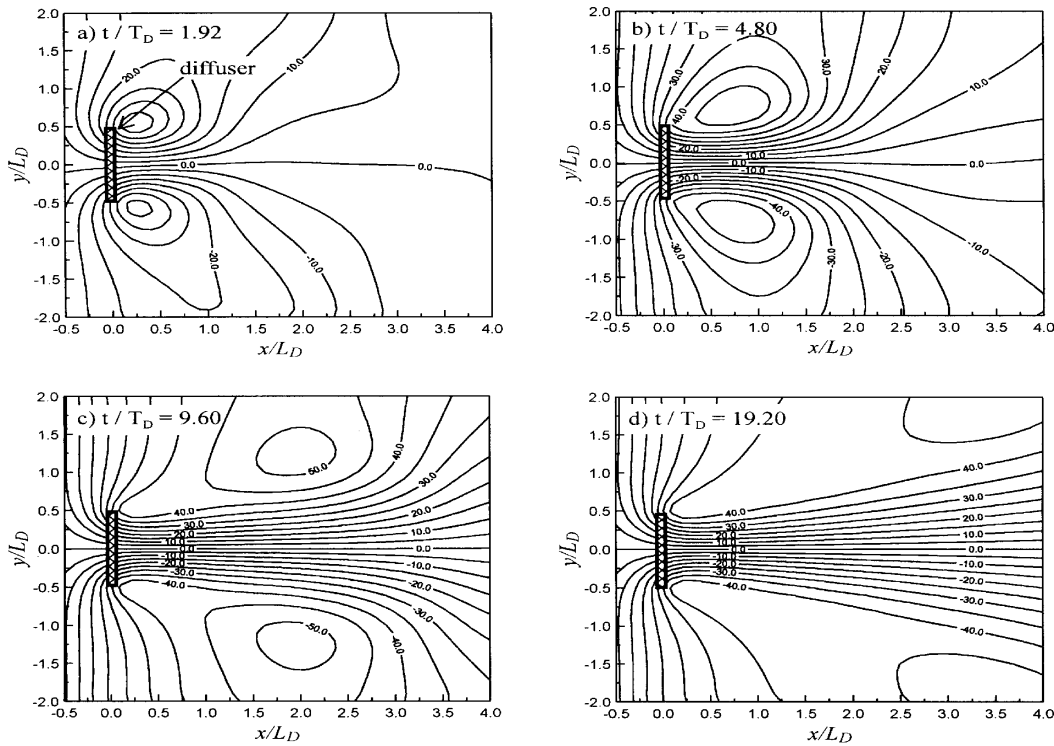


Fig. 7. Streamlines of depth averaged velocity field simulated.

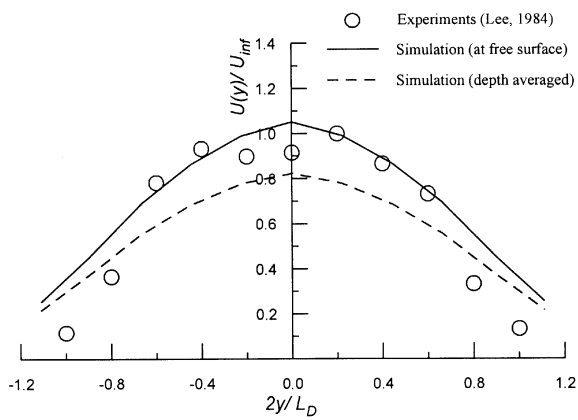


Fig. 8. Comparison of transverse distribution of longitudinal velocity at  $x = L_D$ .

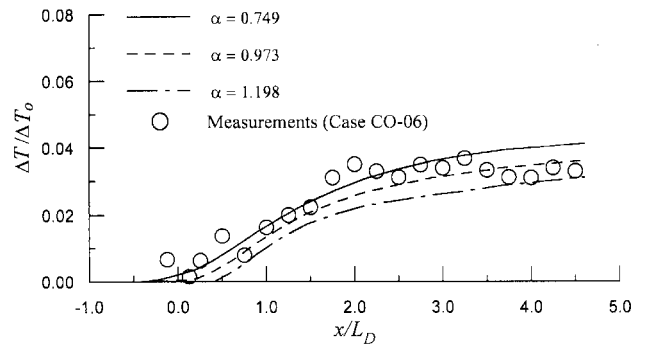


Fig. 9. Longitudinal distributions of dimensionless excess temperature at the water surface with several  $\alpha$  (Case CO-06).

ured or calculated at the steady state and initial ambient temperature. As shown Fig. 6, as the momentum ratio,  $M_j$ , increases, the excess temperature near the diffuser decreases. The minimum surface dilution observed,  $S_m$ , which is defined as the discharge excess temperature ( $\Delta T_o$ ) divided by the highest excess temperature ( $\Delta T$ ), are listed in Table 2. Technically, these were decided choosing the highest closed isotherm at the water surface of a scale greater than the port spacing to eliminate consideration of local hot spots caused by single jets. The observed dilution data collected in this study shows that dilution increases as momentum ratio increases. This is the same results suggested by Adams (1982).

## 4 Numerical modeling

### 4.1 Simulation of velocity distribution

Since detailed velocity data were not collected in this study, experiments conducted by Lee (1984) were used to verify the numerical model for the simulation of velocity fields. Based on Lee's experiments, the distance of shoreline to the location of the diffuser,  $x_s/L_D$ , is approximately 1. Discharge velocity,  $U_o$  of 0.1 m/s is imposed as a plane source and excess temperature is not imposed. A  $51 \times 41$  ( $x$ - $y$ ) orthogonal grid in which for both  $\Delta x$  and  $\Delta y$   $0.11L_D$  is imparted and 0.1 for  $\Delta\sigma$ .  $C_s$  is selected to be 0.3.  $DV_{ref}$  is selected to be  $10^{-5}$  m<sup>2</sup>/s. For the numerical simulation, the no slip condition is imposed at a solid boundary of shoreline. At open boundaries of the other three planes, normal gradient of all other variables is set to zero. As an initial condition, cold start conditions, in which all variables are set to zero is imposed.

Streamlines of depth averaged velocity field computed with time variation are depicted in Fig. 7. Fig. 7a) is the result of  $1.92 T_D$  after, and a pair vortex as suggested in Lee et al. (1996) is located in front of diffuser. Time scale,  $T_D$ , is defined as follows.

$$T_D = \frac{L_D}{U_o} \quad (32)$$

As time progresses, vortices are moved away to the outer region and the slipstream effect of accelerating velocity due to contraction of the streamline is properly simulated. In Fig. 8, transverse distributions of longitudinal velocity at steady state are compared with the results of Lee (1984) at  $x/L_D = 1.0$ . In Fig. 8,  $U_{inf}$  is defined as follows.

$$U_{inf} = \sqrt{\frac{2m_o}{H}} = \sqrt{2}U_o \quad (33)$$

As shown in this figure, the agreement is satisfactory. Both computed and measured velocity distributions tend to follow a symmetrical Gaussian curve.

### 4.2 Simulation of temperature distribution

To simulate the behavior of a coflowing diffuser studied in this experiment, a  $41 \times 21$  ( $x$ - $y$ ) orthogonal grid in which  $\Delta x$  is 0.2 to  $0.8 L_D$ ,  $\Delta y$  is  $0.2 L_D$  and  $\Delta\sigma$  is 0.1 is used. The simulation

is carried out about representative six cases. The no slip condition is imposed at the solid boundary, constant velocity is imposed at the inlet and constant head is imposed at the outlet.  $C_s$  and  $DV_{ref}$  are 0.3 and  $10^{-5}$  cm<sup>2</sup>/s respectively.

In this study, the value of  $\alpha$  which is determined using the CO-06 case is used for all cases. From Fig. 9 in which longitudinal distributions of dimensionless excess temperature ( $\Delta T/\Delta T_o$ ) with several values of  $\alpha$  are shown with measured temperature data at the water surface,  $\alpha$  is selected as 0.973. As explained earlier Fig. 6 shows comparative distributions of experimental and numerical dimensionless excess temperature at the water surface. Shapes of the thermal plume, simulated by the numerical model, are in good agreement with the observed thermal plume. As the momentum ratio,  $M_j$ , increases, the area for excess temperature near the diffuser decreases.

The longitudinal distribution of numerical and experimental dimensionless excess temperature along the centerline of the diffuser at the water surface is depicted in Fig. 10. As shown in Fig. 10, excess temperature decreases with increasing momentum ratio. This result confirms the previous theory proposed by Adams (1982) in which the dilution of a coflowing diffuser, defined as  $\Delta T_o/\Delta T$ , increases with increasing momentum ratio. This indicates that when the ambient current is strong the thermal plume is rapidly swept away from the near field. The simulations by the numerical model are in relatively good agreement with experimental results, especially when the momentum ratio is high. However, when the momentum ratio is low, the measured distribution fluctuates somewhat and deviates from the simulated distributions. This may be due to large scale turbulence generated by strong velocity of the jet discharged from the diffuser.

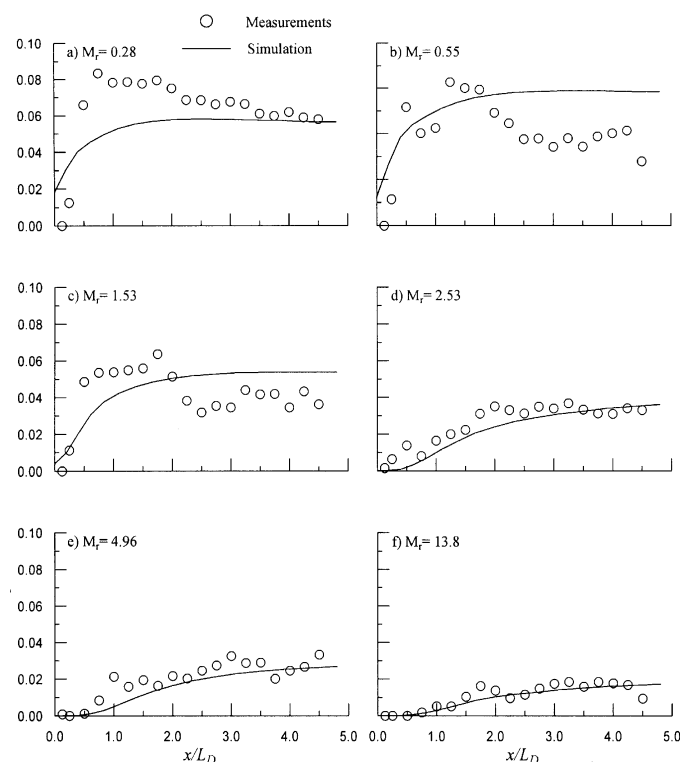


Fig. 10. Longitudinal distributions of dimensionless excess temperature along  $y/L_D = 0$  at water surface

In Fig. 11, transverse distributions of numerical and experimental dimensionless excess temperature at  $x/L_D = 4$  are depicted. Both experimental and simulated distributions tend to follow a Gaussian curve. The comparison shows that the numerical model overshoots measurements when the momentum ratio is low, even though the simulated maximum values at the center of the diffuser are generally in good agreement with the measured values. When the momentum ratio is high, overall distributions of the simulated results agree with the measured distributions.

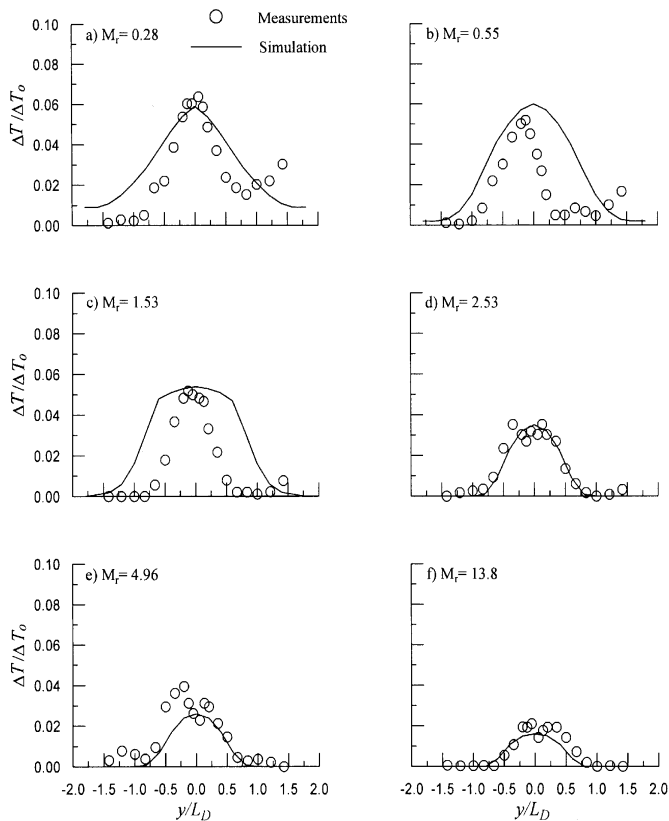


Fig. 11. Transverse distributions of dimensionless excess temperature at  $x/L_D = 4$ .

## 5 Conclusions

Heated water mixing as the result of discharge from a submerged multiport diffuser was analyzed using the three-dimensional grid-based numerical model in which discharge momentum flux is properly considered using the concept of a numerical slot diffuser, along with multi-jet theory. The proposed model properly simulates velocity induced by a coflowing diffuser in proximity to a shoreline boundary, and this is confirmed by Lee's experiments. A comparison of model simulations with laboratory experiments shows that the shapes of thermal plume simulated by the numerical model are in good agreement with the observed thermal plume. A comparison of longitudinal distributions of numerical and experimental dimensionless excess temperature along the centerline of the diffuser at the water surface shows that dilution of the coflowing diffuser increases with increasing momentum ratio because the

thermal plume is swept away rapidly from the near field due to strong ambient current. The simulations by the numerical model are in relatively good agreement with experimental results, especially when the momentum ratio is high. A comparison of transverse distributions of numerical and experimental dimensionless excess temperature shows that both experimental and simulated distributions tend to follow a Gaussian curve and the results of the numerical model are generally in good agreement with the measured values.

## 6 Acknowledgements

This research work was partially supported by the 1995 Non Directed Research Fund of Korea Electric Power Corporation, Seoul, South Korea. The authors are grateful to Hong-Sik Kim for his help in the laboratory work.

## 7 Symbols

$b$	effective width of single jet
$B$	width of equivalent slot diffuser
$C_s$	Smagorinsky's constant
$DV_{ref}$	base vertical eddy viscosity and diffusivity
$E_v$	vertical eddy diffusivity
$f$	Coriolis' constant
$F_s$	discharge densimetric Froude number of equivalent slot diffuser
$g$	gravitational acceleration
$g'_o$	effective gravitational acceleration
$G_H$	Richardson number
$h$	bottom topography
$I_q$	shape constants
$j_o$	discharge buoyancy flux per unit length
$K_H$	horizontal eddy viscosity
$K_q$	vertical eddy diffusivity in transport equation for turbulence characteristics
$K_V$	vertical eddy viscosity
$l$	turbulence length scale (in section 2.2) port spacing (in section 2.3)
$l_q$	characteristic length scale
$L_D$	diffuser length
$m_o$	discharge momentum flux per unit length
$M_r$	momentum ratio of the ambient current to the effluent discharge
$n$	number of ports in a cell of numerical slot diffuser
$q^2$	two times turbulent kinetic energy
$Q_o$	discharge flowrate from ports in a cell of numerical slot diffuser
$Q_N$	discharge flowrate from a cell of numerical slot diffuser
$S_m$	minimum surface dilution
$T$	temperature
$u_a$	ambient current velocity
$U_c$	jet centerline velocity
$U_o$	outlet velocity
$U, V, W$	velocity component at Cartesian coordinate

$\tilde{W}$	wall proximity function
$x, y, z$	Cartesian coordinate
$x, y, \sigma$	transformed coordinate
$x_s$	distance of shoreline to location of diffuser
$\Delta T$	excess temperature
$\Delta T_N$	discharge excess temperature from numerical slot diffuser
$\Delta T_o$	discharge excess temperature from multiport diffuser
$\alpha$	coefficient of proportionality
$\kappa$	von Karman constant
$\rho$	density
$\rho_o$	reference density
$\tau_b$	bed shear stress
$\tau_w$	wind shear stress
$\Omega$	velocity in $\sigma$ direction
$\zeta$	water surface elevation

## 8 References

- [1] ADAMS, E.E. (1982), Dilution analysis for unidirectional diffusers., *J. of hydraulic division*, ASCE, Vol. 108, No. HY3, pp. 327-342
- [2] AKAR, P.J., and JIRKA, G.H. (1991), *CORMIX2: An expert system for hydrodynamic mixing zone analysis of conventional and toxic multiport diffuser discharges.*, Defrees hydraulics laboratory, School of civil and environmental engineering, Cornell university, Ithaca, New York.
- [3] BAUMGARTNER, D.J., TRENT, D.S., and ROBERTS, P.J.W. (1993), *Dilution models for effluent discharges (2<sup>nd</sup> ed.)*, EPA/600-R-93/139, U.S. EPA.
- [4] BLUMBERG, A.F., GALPERIN, B., and O'CONNOR, D.J. (1992), "Modeling vertical structure of open-channel flows." *J. of hydraulic engineering*, ASCE, Vol. 118, No. 8, pp. 1119-1134.
- [5] BLUMBERG, A.F., and MELLOR, G.L. (1987), "A description of a three-dimensional coastal ocean circulation model." in *Coastal and estuarine sciences* 4, American geophysical union, pp. 1-16.
- [6] CHENG, R.T., and SMITH, P.E. (1989), "A survey of three-dimensional numerical estuarine models." Proc. of the conference estuarine and coastal modeling, edited by M.L. Spaulding, Newport, Rhode Island, pp. 1-15.
- [7] DAVIES, A.M., JONES, J.E., and XING, J. (1997 a, b), "Review of recent developments in tidal hydrodynamic modeling. I: Spectral models., II: Turbulence energy models" *J. of hydraulic engineering*, ASCE, Vol. 123, No. 4, pp. 278-302.
- [8] ECKART, C. (1958), "Properties of water, Part II. The equation of state of water and sea water at low temperatures and pressures." *American J. of science*, Vol. 256, pp. 225-240.
- [9] FISCHER, H.B., LIST, E.J., KOH, R.C.Y., IMBERGER, J., and BROOKS, N.H. (1979), *Mixing in inland and coastal waters.*, ACADEMIC PRESS.
- [10] GALPERIN, B., KANTHA, L.H., HASSID, S., and ROSATI, A. (1988), "A quasi-equilibrium turbulent energy model for geophysical flows." *J. of the atmospheric science*, Vol. 45, pp. 55-62.
- [11] JIRKA, G.H. (1982), "Multiport diffusers for heat disposal: a summary." *J. of hydraulics div.*, ASCE, Vol. 108, No. HY12, pp. 1425-1468.
- [12] JIRKA, G.H., and HARLEMAN, D.R.F. (1973), *The mechanics of submerged multiport diffusers for buoyant discharges in shallow water.*, Technical report No. 169, Ralph M. Parson laboratory for water resources and hydrodynamics, M.I.T.
- [13] LEE, J.H.W. (1984), "Boundary effects on a submerged jet group." *J. of hydraulic research*, Vol. 22, No. 4, pp.199-216.
- [14] LEE, J.H.W., RODI, W., and WONG, C.F. (1996), "Turbulent line momentum puffs." *J. of engineering mechanics*, ASCE, Vol. 122, No. 1, pp. 19-29.
- [15] ROBERTS, P.J.W., SNYDER, W.H., and BAUMGARTNER, D.J. (1989 a, b, c), "Ocean outfalls. I: Submerged waste field formation., II: Spatial evolution of submerged wastefield., III: Effect of diffuser design on submerged wastefield." *J. of hydraulic engineering*, ASCE, Vol. 115, pp. 1-70.
- [16] WOOD, I.R., BELL, R.G., and WILKINSON, D.L. (1993), *Ocean disposal of wastewater.*, World Scientific, Singapore.

